THE ASTROPHYSICAL JOURNAL, 427:L83–L86, 1994 June 1

FIRST DETECTION OF A GRAVITATIONAL WEAK SHEAR AT THE PERIPHERY OF CL 0024+1654[1]

HENRI BONNET, YANNICK MELLIER, AND BERNARD FORT
Laboratoire d'Astrophysique de Toulouse, Observatoire Midi-Pyrénées, 14 Avenue E. Belin, F-31400 Toulouse, France
Received 1994 January 8; accepted 1994 March 11

ABSTRACT

We report on the first measurement out to 1.5 h_{100}^{-1} Mpc from the center of a coherent gravitational shear of faint objects around the cluster lens Cl 0024+1654. Ultra-deep CCD images taken in subarcsecond seeing conditions at the Canada-France-Hawaii Telescope show biased distributions of ellipticity and orientation that are interpreted as gravitational distortion of the observed images of background sources by the cluster. The shear intensity decreases radially, and from its pattern we infer that the center of the mass distribution coincides with the optical center. Assuming a power law for the projected mass profile, we constrain its slope to range between 0.7 and 1.2. The data are compatible with the Isothermal Sphere (IS) model, although a de Vaucouleur law (dVc) reasonably fits the observations. For the IS model, the core radius is below 20″, with marginal agreement out to 40″, and no cutoff radius is seen in the range of the data. The two models may be distinguished by measuring the shear field beyond 15′ with twice the present accuracy. The total mass within an Abell radius reaches the large value of $2 \times 10^{15}\ h_{100}^{-1}\ M_{\odot}$ (IS) or $1.2 \times 10^{15}\ h_{100}^{-1}\ M_{\odot}$ (dVc). We predict the typical redshift of sources to be $z = 0.7$–0.8 for the IS but $z > 1.2$ for dVc.

Subject headings: galaxies: clusters of — gravitational lensing

1. INTRODUCTION

The discovery of faint arclets in A370 (Fort et al. 1988) confirmed that distant galaxies can be weakly lensed by rich clusters (see Webster 1985; Grossmann & Narayan 1988). Tyson, Valdes, & Wenk (1990) first used the analysis of arclets distribution to probe the dark matter in the center of A1689. Miralda-Escudé (1991) and Kaiser & Squire (1993) show that cluster mass distributions can be inferred from weak shear analysis. Thus weak lensing can complement the inner mass distribution inferred from giant arcs. Good candidates are clusters with multiple arcs for which well-constrained models exist, such as Cl 0024+1654 (Kassiola, Kovner, & Fort 1992, hereafter KKF). In addition, it is rich, rather regular, with a large angular size, and its outer regions are not crowded by cluster members. It also crosses the zenith at the CFHT latitude, which guarantees the best image quality. In this *Letter* we describe the analysis of the shear field and the mass profile of Cl 0024+1654.

2. OBSERVATIONS

Observations were run at the prime focus of the CFHT in 1991 November and 1992 November, in photometric conditions and with seeings ranging from 0.″55 to 0.″7. The first run was dedicated to the inner region of the cluster. A total integration time of 4.5 hr in the B bandpass was obtained, using the 640 × 1024 RCA2 CCD with a scale of 0.″2 pixel^{-1}. Additional I images with the 2048 × 2048 (LORAL2 CCD at the same resolution were obtained with the same exposure time. Details of these observations are in KKF. During the second run, we minimized the atmospheric refraction by using the V band with the Lick2 CCD and restricting observations to ±1.5 hr from the meridian. We integrated 7 × 45 mn, with random shifts of 10″, on an external region extending out to 10′ from the center, and overlapping the central field. The data prereduction including sky-flattening and the final co-added images were produced by IRAF. As the flat fields are not integrated strictly under the same atmospheric conditions during the run, some residual large-scale fluctuation of the sky contribution might affect the image even after prereduction. Simulations show that sky variations of 20% on scales of 100″ can induce a shear effect of 5%. We applied a low bandpass filter to remove this (see Bonnet & Mellier 1994, hereafter BM) and checked that the effect was eliminated.

3. DETECTION OF THE SHEAR FIELD IN CL 0024+1654

The detection algorithms and the shear measurement are described in BM. Let $sh = 1 - e$ and θ_s be the shear intensity and orientation, where e and θ_s are the axis ratio and the orientation of the image of a lensed circular source. In terms of K and γ (Kneib et al. 1994), $sh = -4K\gamma/(K - \gamma)^2$. We measure with precision the shape parameters of faint background objects, eliminating any atmospheric or instrumental contributions. Using classical detection criteria, ∼1550 objects are found on the central field, with $20 < B < 28$, and 2900 objects on the eastern field, with $20 < V < 28$. Shape parameters are computed through a constant aperture (see BM). This preserves the orientation of objects but, together with the seeing effect, leads to a systematic underestimation of ellipticities. Pixelization has no significant effect because objects are large enough (∼10 pixels).

Elongation due to (1) atmospheric refraction, (2) flaws in telescope optics, (3) bad tracking, or (4) errors during data prereduction when matching shifted images can induce spurious elongations on the images. The analysis of a stellar field shows that effects 1 and 2 are small. Effects 3 and 4 need to be measured straight from the image and cannot be separated. Each of them can be modeled as a

[1] Based on the observations at the Canada-France-Hawaii Telescope (CFHT).

thin lens and their combination can be evaluated, by using bright unsaturated stars, selected by eye, and computing their average shape matrix, that is, the square of their "shear" matrix. The lens equation dan then be inverted, if one of the effects dominates, or if their contributions are parallel, and the correction can be applied on shape matrices of galaxies. Since the shear is weakly distorting sources that have their own shape, and since the images are faint, individual images are meaningless. We cancel the contribution of source ellipticities and improve the S/N by co-adding shape matrices within superpixels, with typical size 1 arcmin^2, smaller than the typical scale of variation of the shear. The average shape matrix gives the local shear, assuming that sources (1) are uniformly oriented and (2) have the same redshift. Hypothesis (2) is valid because for a single lens, the shear orientation does not depend on redshift, and its intensity far from critical lines slowly increases with z. The convergence toward the local shear matrix is theoretically exact (see BM): the contribution of the shape matrix is a linear function of brightness, as the lens equation is. Thus co-adding images leads to the same result as lensing a sum of sources. Invoking, hypothesis (1) implies that the result is the shape matrix of a lensed circular source. We evaluate the significance of the detection from the dispersion of θ_s with respect to the orthoradial direction, over the full set of superpixels.

The seeing effect together with the use of a circular aperture imply that the shear intensity is underestimated. Corrections are performed to account for these effects using simulations of CCD images of galaxies with constant ellipticity, which reproduce the same observing conditions, including seeing and photon noise. This suppresses the internal dispersion of the measure due to the ellipticity distribution in the source plane and allows an accurate determination of the correction. We find a typical correction factor of 4 for weak shear of 10%. An empirical relation ($sh_{obs} \leftrightarrow sh_{real}$) is thus established.

4. ANALYSIS OF CL 0024+1654

4.1. *Evaluation of the Shear and Errors*

Figure 1 (Plate L5) shows that our algorithm detects the shear almost everywhere up to 10′ from the center. For each superpixel, we computed $\Delta\theta$, the deviation of the measured orientation from the tangential direction with respect to the optical center of the cluster. We then estimate the significance level as the probability for a larger value of $\langle\Delta\theta^2\rangle$ to occur with a random distribution. We find it to be better than 95%, and the results are consistent from one image to the other although they correspond to different observing conditions, with various orientations and filters.

The B image covers a 3.20 × 4.10 arcmin^2 field and is divided into two parts separately integrated during a single CFHT run. The eastern part needs a small correction in the N-S direction, while the western part shows an instrumental distortion of ~5% parallel to the N-NE direction. Objects of the B image were selected with axis ratios ranging from 0.6 to 0.8, and co-added in bins of 50. The correlation of orientation from bin to bin indicates a high S/N. Analysis of the I image gives a similar shear pattern, although the star distortion is not constant over the CCD (we discarded these I data for the rest of the analysis). Since the V frame covers an area farther from the center, the shear is hardly detected when correction is neglected. Nineteen bright unsaturated stars were detected on this image. Co-adding them in bins of four, with 50% overlap between two neighboring bins, we find an rms fluctuation of 6°.5 in the orientation, and 0.3% in the axis ratio for the whole frame. These fluctuations are due to the small number of stars per bin that were used. As no coherent evolution of the stars elongations is seen along the frame, we conclude that the correction to apply does not significantly depend on the position, and therefore we co-added the 19 stars to improve the accuracy of the correction. We find an average distortion of 1.3% in the E-W direction due either to tracking problem, or to imprecision when co-adding images. After correction, a coherent shear is clearly detected up to 10′ from the center. The best S/N is obtained when objects are selected with axis ratio ranging from 0.7 to 0.9 which is slightly less elliptical than for the B frame.

Note a perturbation in the upper left part of the image. The projected mass distribution of this structure seems almost circular and can be well fitted by a singlar isothermal model (SIS). We do not know whether it is a substructure of Cl 0024 or an independent gravitational system projected on the line of sight. It would be interesting to investigate spectroscopically this part of the field to confirm the efficiency of our technique in detecting substructures in clusters. Except for this perturbation, the shear patterns detected in the B and I central fields and in the V eastern are almost circular.

The analysis of a stellar field (NGC 2264) with the same observing conditions gives an atmospheric-instrumental shear pattern with constant E-W direction of elongation, consistent with the results on the 19 selected stars of the eastern Cl 0024 field. We therefore believe that the shear observed on this field is real.

4.2. *Determination of the Center and Radial Behavior of the Shear*

BM give a procedure to estimate the center of the potential only from the weak shear field (without using the giant arcs). Figure 2 (Plate L6) shows the isoprobability contours obtained from the B image. The best position is only 1″ off the optical center, defined by the position of the brightest galaxy. Similar results are found by Tyson et al. (1990).

The radial behavior of the shear is computed from the center through the following process: we first eliminate the area of the perturbation on the northern part of the V image. We then compute the mean values of the shape matrix in concentric annuli. Before adding matrices up, we rotate each of them in their orthonormal frame which is defined with respect to the center of the cluster, to account for the evolution of the shear direction. Figure 3 shows the result with 1 σ error bars when objects are binned in groups of 200. Clearly, the shear is monotonically decreasing from the center. The measure is significant up to 7′ from the center. The uncertainties have been estimated by comparing the observed result to draws in which the correlation between orientation and ellipticity is broken by randomly redistributing the object orientations, keeping the ellipticity distribution unchanged. In most cases the information on the shear is lost: the mean matrix has random orientation, and the co-added axis ratio is close to unity. The rms fluctuation of the mean axis ratio obtained from 100 draws is equal to the internal dispersion we would observe in the absence of shear and is therefore taken as the error. To check the consistency of our correction method we simulated CCD images, with a constant shear, including the random distribution of ellipticity in the source plane. We found after analysis and correction, the correct value for the shear, with the same error bars as for the real data.

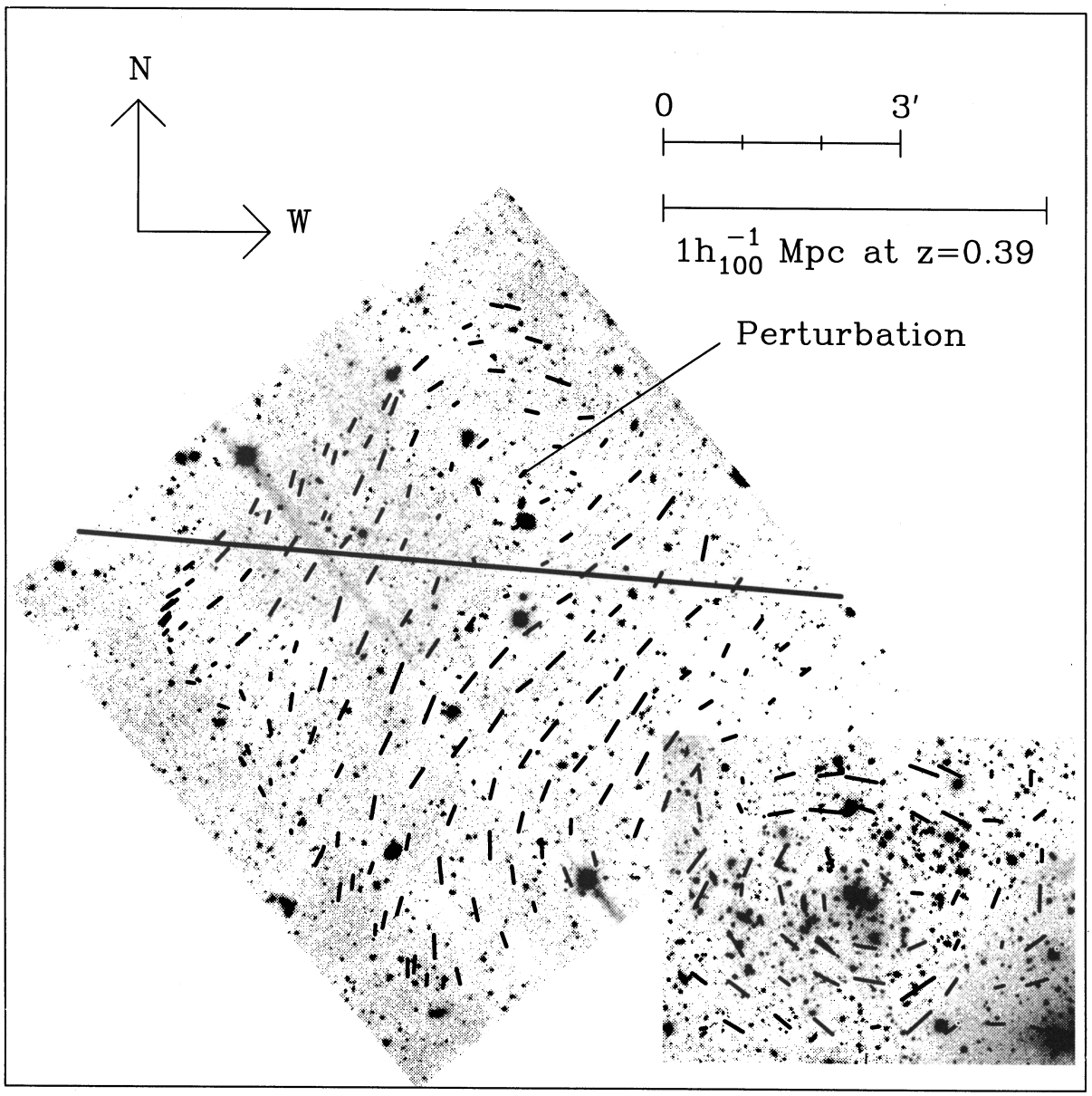

FIG. 1.—Shear pattern in Cl 0024. The *B* central field is at the bottom-right; black segments show the local orientation of the shear, and their length is proportional to the shear intensity (arbitrary scales for each field). A large perturbation to the cluster potential, associated with a local substructure, can be seen in the eastern field. This region, north of the horizontal line, was discarded for the measure of the radial evolution of the shear.

BONNET, MELLIER, & FORT (see 427, L84)

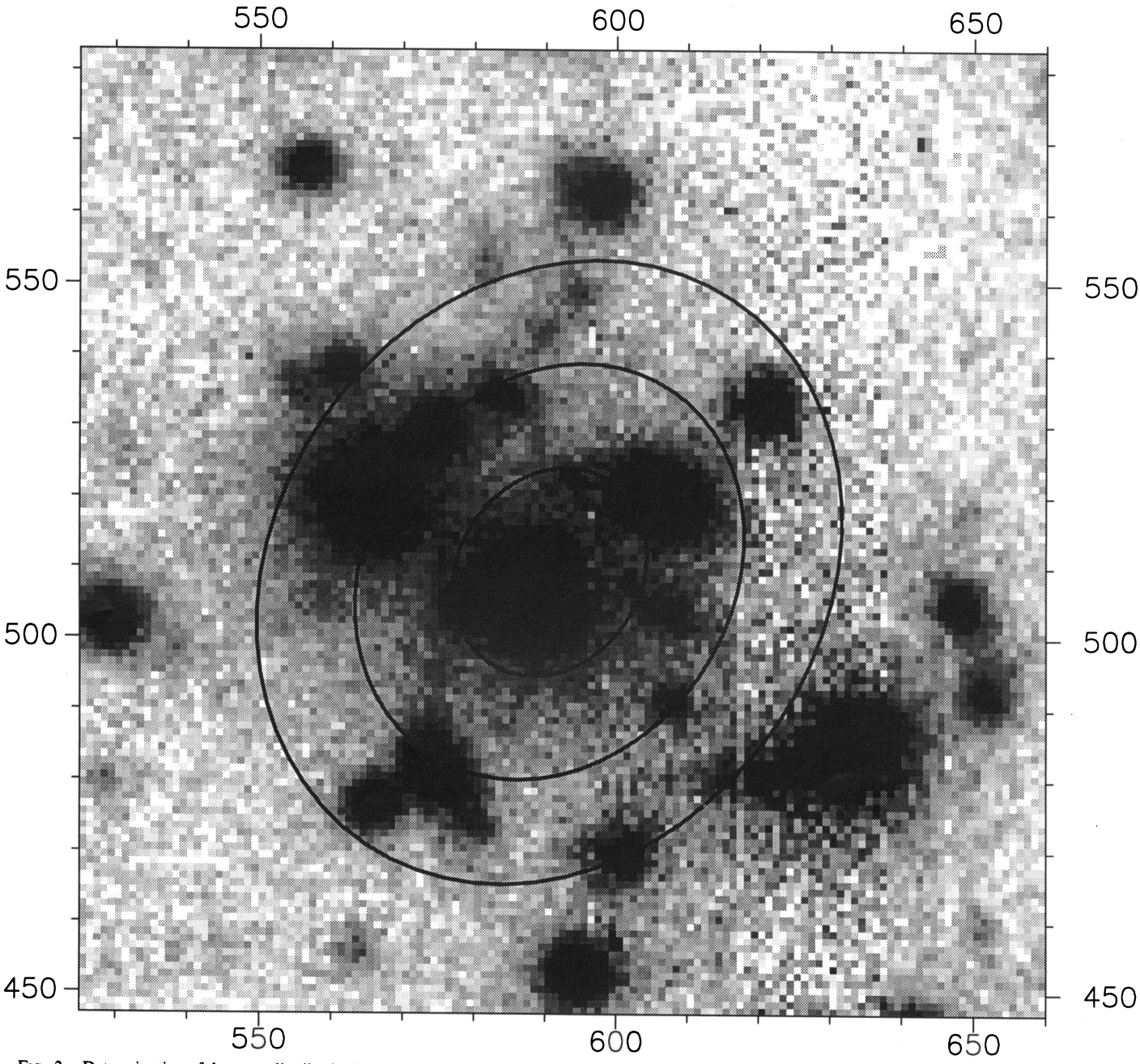

FIG. 2.—Determination of the mass distribution's center from the shear distribution in Cl 0024. The central field only was used. Objects were selected using their ellipticities and central brightnesses. Ellipses show the 1, 2, and 3 σ isoprobability contours. Their axis ratios and orientation depend on the variations of the signal-to-noise ratio along the field and are not connected to the ellipticity of the potential.

BONNET, MELLIER, & FORT (see 427, L84)

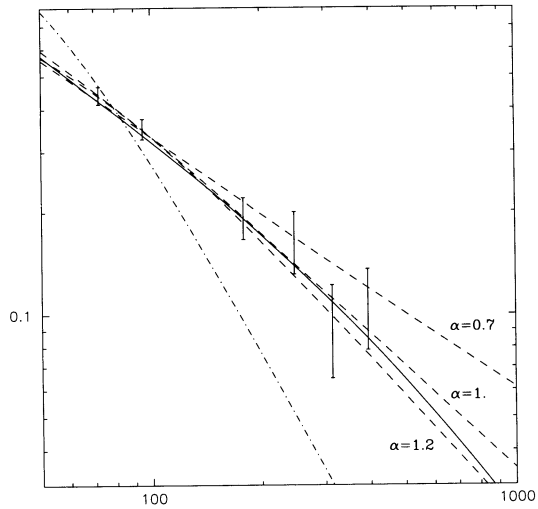

FIG. 3.—Measure of the shear for Cl 0024. Objects were radially binned in groups of 200 for the eastern field, and 50 for the central one. Error bars show 1 σ deviations. The two points on the left are for the *B* central field, and the rest are for the *V* eastern field. Best fits are also plotted for de Vaucouleur (dVc) profile (*solid line*), power-law models of various slopes (*dashed lines*), and point mass model (*dashed-dotted line*).

5. COMPARISON WITH MASS PROFILES

We compare the observed radial behavior of the shear with that inferred for different spherically symmetric mass distributions. From Figure 3 we see that the expected shear for a point mass model decreases more steeply than the measured data and cannot fit the data on scales ranging from 100″ to 400″. This confirms that there is a significant contribution to the total mass lying farther than 100″ from the center.

We test simple power-law surface mass distributions: $\Sigma(r) = \Sigma_0 r^{-\alpha}$. For each value of α, an optical value of Σ_0 is determined by χ^2 minimization. Acceptable fits are obtained for $0.7 < \alpha < 1.2$, with the best-fit close to the SIS ($\alpha = 1$). We next consider more realistic power-law models with core radius (hereafter PLCR) and central surface density $\Sigma_{\rm pl}$ and compare them to de Vaucouleur (dVc) models $\Sigma_{\rm dVc}$:

$$\Sigma_{\rm pl} = \frac{8\alpha\sigma^2}{3\pi G r_c}\frac{I^2_{(1+\alpha)/2}}{I_\alpha}, \qquad \Sigma(r) = \Sigma_{\rm pl}\frac{1 + (1 - \alpha/2)(r/r_c)^2}{[1 + (r/r_c)^2]^{1+\alpha/2}}. \tag{PLCR}$$

For $r \gg r_c$, $\Sigma_{\rm pl}$ scales as $r^{-\alpha}$. The total mass is infinite for $\alpha \leq 2$, but at a given radius, the shear is only sensitive to the mass interior to this radius, which is finite. PLCR scales as $r^{-\alpha}$, σ is the observed velocity dispersion, and r_c the core radius. $I_\beta = \int_0^\infty (1 + u^2)^{-\beta}\, du$;

$$\Sigma_{\rm dVc} = \frac{9\gamma^8\sigma^2}{8\pi G C(\mu) 7! r_e}, \qquad \Sigma(r) = \Sigma_{\rm dVc}\exp\left[-\gamma\left(\frac{r}{r_e}\right)^{1/4}\right], \tag{dVc}$$

where r_e is the effective radius, $\gamma = 7.67$, and σ is the observed velocity dispersion. $C(\mu)$ accounts for the fact that the shear is measured over a finite area of size μ (Wu 1993). The corresponding expressions for the shear are, respectively:

$$sh_{\rm pl}(s) = 1 - \frac{1 - \varphi_{\rm pl}[(1 + s^2)^{-\alpha/2}]}{1 - \varphi_{\rm pl}\{(1 + s^2)^{-(1+\alpha/2)}[1 + (1 - \alpha)s^2]\}}, \qquad \varphi_{\rm pl} = \frac{2\pi G}{3[1 - (\alpha/2)]c^2}\frac{D_{\rm LS}}{D_{\rm OS}}\Sigma_{\rm pl} r_c,$$

$$sh_{\rm dVc}(s) = 1 - \frac{1 - \varphi_{\rm dVc}[e^{-t} - (4/\gamma^8 s^2)\Gamma(8, t)]}{1 - \varphi_{\rm dVc}(4/\gamma^8 s^2)\Gamma(8, t)}, \qquad \varphi_{\rm dVc} = \frac{4\pi G}{c^2}\frac{D_{\rm LS}}{D_{\rm OS}}\Sigma_{\rm dVc};$$

s is the radius scaled to the core (effective) radius. Indices L, O, and S denote, respectively, the lens, the observer, and the source, D_{ij} the angular distance i–j, $t = s^{0.25}$. We impose $\sigma = 1300 \pm 100$ km s^{-1} (Dressler, Gunn, & Schneider 1985) and the existence of a critical radius for $r \sim 35''$ corresponding to the triple arc position with an assumed redshift for its source around 1.3 (Mellier et al. 1991). This is not a severe constraint, but it ensures the consistency of our fits with the observations (actually, similar analysis could be performed on arcless clusters).

Figure 3 plots the best fits for the different models. For the PLCR, the best fit ($\alpha = 1$) matches the observations well, and its parameters are close to the KKF model. Again steeper models ($\alpha > 1.2$) are firmly rejected, Thus, the IS with the core radius proves consistent with the data for both the strong lensing regime (triple arc) and the weak shear up to $1.5\, h_{100}^{-1}$ Mpc from the center. Figure 3 also shows the good agreement of a dVc profile with the data, with an effective radius of 600″.

The models can constrain the redshift distribution of the source as well as the scale factor r_c (PLCR) or r_e (dVc). Figure 4 plots χ^2 against velocity dispersion and z_s for a PLCR with $\alpha = 1$ (IS) and a dVc profile. We find $z_s \sim 0.7$–0.8 for the IS model, in agreement with the value obtained from faint galaxy spectroscopic surveys (Colless et al. 1993; Lilly 1993; Tresse et al. 1993) or arclet redshifts (Kneib et al. 1994). The maximum value for the core radius is 40″, but the agreement between the data and the models is marginal for $r_c > 20''$. Below this value, the models become insensitive to the exact value of r_c. For the dVc model, good fits require $z_s > 1.2$

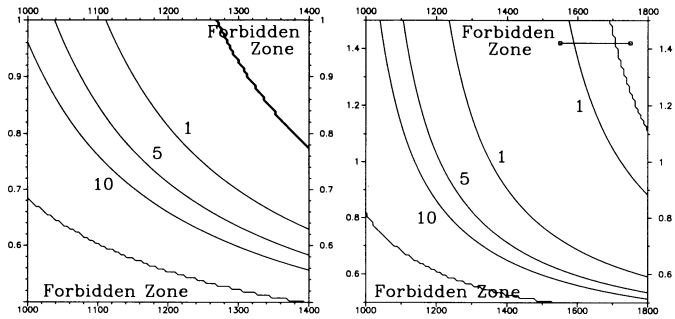

FIG. 4.—Reduced χ^2 vs. σ and z_s for the Isothermal sphere model (*left*) and the de Vaucouleur model (*right*). Numbers are the values of χ^2 for the different isocontours. Forbidden zones correspond to sets of parameters for which there is no critical line at $z = 1.3$ between 20″ and 40″. For power-law models this constraint rejects some models with $z > 0.8$ and $\sigma > 1300$ km s^{-1}, although they fit the data very well ($\chi^2 < 1$).

and $\sigma_0 \sim 1400$ km s^{-1} in marginal agreement with the Dressler et al. (1985) value, but we cannot discriminate between IS and dVc models.

Extrapolating both the IS and the dVc models (Fig. 3) shows that a difference could be seen beyond a radius of 1000″. But at this radius the expected shear in both cases falls below our present detection limit ($sh_{IS} \sim 4\%$; $sh_{dVc} \sim 3\%$).[2] In fact, we expect a cutoff radius R_C in the IS case to ensure a finite total mass. The introduction of a cutoff radius does not affect the central distribution. Thus we ignore the previous constraint on the velocity dispersion and take the simple form for an IS with cutoff radius R_C: $\Sigma(r) = \Sigma_0 r^{-1}\{1 - [1 + (R_C/r)^2]^{-1/2}\}$ where Σ_0 again is a free parameter. We tested χ^2 versus R_C and found that χ^2 is decreasing with R_C along the data interval and remains stable otherwise. The best fit is obtained for $R_C = 700''$ beyond our data interval. As the shear is sensitive to R_C only for $r > R_C$, this shows that R_C is greater than 400″ (1.4 h_{100}^{-1} Mpc). Extrapolating the shear profiles to larger distances shows that within our detection limits, dVc and IS models could be distinguished if $R_C < 500''$.

6. CONCLUSIONS

Our investigation shows that we can detect and measure shear as weak as 5% around gravitational structures. The study of the outermost regions in Cl 0024+1654 enables us to determine observationally the center and the projected mass density profile, and to detect possible substructures in distant rich galaxy clusters. Given a precise model for the mass profile, the average source redshift can also be inferred, as well as a maximum value for the core radius for IS models, and a minimum value for the cutoff radius.

The shear measured for Cl 0024 is compatible with an IS or a dVc law for the mass distribution. Using the IS, with a cutoff radius greater than 400″, the shear profile detected in Cl 0024+1654 up to 1.5 h_{100}^{-1} Mpc gives a minimum total mass of $2 \times 10^{15}\, h_{100}^{-1}\, M_\odot$. This is 3 times larger than the virial mass or the mass inferred by Schneider, Dressler, & Gunn (1986) within the same radius, corresponding to a mass-to-light ratio larger than 1000 h_{100}! Similar estimates are found by Smail et al. (1994) and Fahlman et al. (1994). The dVc model predicts a mass of only $1.2 \times 10^{15}\, h_{100}^{-1}\, M_\odot$, within the same radius. This lower determination is due to the fact that this model predicts a higher redshift for the sources. Our detection technique remains sensitive for shear values down to 5%, which is what we expect for an IS at $\sim$700″ (2.5 h_{100}^{-1} Mpc). If the mass density profile remains isothermal at this distance, the total would be incredibly high ($4 \times 10^{15}\, h_{100}^{-1}\, M_\odot$). This result urges to be confirmed by observing the shear field all around the cluster center, and at even larger radii than our present data. Observations of the cluster velocity dispersion out to similar radii are also in progress.

The minimum shear intensity we detect now (5%) is not far from the 1% level required to investigate large-scale structures (Blandford et al. 1991; Kaiser 1992). However, substantial improvements of the method should be implemented.

Part of this work was supported by the French CNRS and resulted from the ESO key program 015-001-45K "arc survey" and the CFHT complementary "arc survey" program. We thank P. Y. Longaretti for his imaginative and fruitful suggestions and I. Kovner for numerous discussions and advice.

[2] Separation between the two models could also be done by observing the behavior of σ with radius out to $\sim$800″ (Wu 1993) or by extending redshift surveys to very faint magnitudes, in order to measure the source redshift distribution.

REFERENCES

Blandford, R. D., Saust, A. B., Brainerd, T. G., & Villumsen, J. V. 1991, MNRAS, 251, 600
Bonnet, H., & Mellier, Y. 1994, in preparation (BM)
Colless, M. M., Ellis, R. S., Broadhurst, T. J., Taylor, K., & Peterson, B. A. 1993, MNRAS, 2261, 19
Dressler, A., Gunn, J. E., & Schneider, D. P. 1985, ApJ, 294, 70
Fahlman, G. G., Kaiser, N., Squires, G., & Woods, D. 1994, ApJ, submitted
Fort, B., Prieur, J. L., Mathez, G., Mellier, Y., & Soucail, G. 1988, A&A, 200, L17
Gross, S. A., & Narayan, R. 1988, ApJ, 324, L37
Kaiser, N. 1992, ApJ, 388, 272
Kaiser, N., & Squire, G. 1993, ApJ, 404, 441
Kassiola, A., Kovner, I., & Fort, B. 1992, ApJ, 400, 41 (KKF)
Kneib, J.-P., Mathez, G., Fort, B., Mellier, Y., Soucail, G., & Longaretti, P.-Y. 1994, A&A, in press
Lilly, S. 1993, ApJ, 411, 501
Mellier, Y., Fort, B., Soucail, G., Mathez, G., & Cailloux, M. 1991, ApJ, 380, 334
Miralda-Escudé, J. 1991, ApJ, 380, 1
Schneider, D. P., Dressler, A., & Gunn, J. E. 1986, AJ, 92, 523
Smail, I., Ellis, R., Fitchett, M., & Edge, A. C. 1994, MNRAS, submitted
Tresse, L., Hammer, F., Le Fèvre, O., & Proust, D. 1993, A&A, 277, 53
Tyson, J. A., Valdes, F., & Wenk, R. A. 1990, ApJ, 349, L1
Webster, R. L. 1985, MNRAS, 213, 871
Wu, X. P. 1993, ApJ, 411, 513